Increasing the Accuracy of Electromagnetic Inverses Using Functional Area Source Correlation Constraints

Benoit R. Cottereau*, **Justin M. Ales**, **and Anthony M. Norcia**

Department of Psychology, Stanford University, Stanford, California

Abstract: Estimating cortical current distributions from electroencephalographic (EEG) or magnetoencephalographic data is a difficult inverse problem whose solution can be improved by the addition of priors on the associated neural responses. In the context of visual activation studies, we propose a new approach that uses a functional area constrained estimator (FACE) to increase the accuracy of the reconstructions. It derives the source correlation matrix from a segmentation of the cortex into areas defined by retinotopic maps of the visual field or by functional localizers obtained independently by fMRI. These areas are computed once for each individual subject and the associated estimators can therefore be reused for any new study on the same participant. The resulting FACE reconstructions emphasize the activity of sources within these areas or enforce their intercorrelations. We used realistic Monte-Carlo simulations to demonstrate that this approach improved our estimates of a diverse set of source configurations. Reconstructions obtained from a real EEG dataset demonstrate that our priors improve the localization of the cortical areas involved in horizontal disparity processing. *Hum Brain Mapp 33:2694–2713, 2012.* © 2011 Wiley Periodicals, Inc.

Key words: electromagnetic brain imaging; EEG; vision; retinotopy; fMRI

INTRODUCTION

The reconstruction of cortical current distributions from electroencephalographic (EEG) and magnetoencephalographic (MEG) data can be approached as an imaging problem where the unknown sources are distributed on an individual's cortex with their orientations fixed and normal to the local surface [Dale and Sereno, 1993]. Several thousand sources are necessary to model the convolutions of the cortical manifold precisely, but only a hundred or so measurements are available. The associated inverse procedure is thus severely ill-posed and has no unique solution [Hämäläinen et al., 1993]. Conventional approaches to this issue introduce priors on the source distribution to constrain the estimation problem. While there are many sorts of priors invoked in EEG/MEG source imaging, a typical requirement for a straightforward inverse procedure is that the current distribution be spatially smooth and follow a Gaussian distribution with zero mean and a covariance matrix $\mathbf{R}$. If this covariance matrix is proportional to the identity matrix, several different approaches exist to define it [Baillet et al., 2001]. Some estimators have a bias towards superficial currents, associated with the attenuation of the MEG and EEG lead fields with increasing source depth. To circumvent this superficial bias, some studies have proposed a modification of the diagonal elements of the source-covariance matrix $\mathbf{R}$ using for each

source a scaling parameter determined by a function of the distance to the sensors [Jeffs et al., 1987; Lin et al., 2006]. Using a reweighting algorithm that iteratively redefined the matrix **R**, Gorodnitsky et al. provided another solution to this bias [Gorodnitsky et al., 1995; see also Moran et al., 2005 for a multiresolution implementation of the algorithm]. Their method also limited the over-estimation of the spatial extent of the activity inherent to L2-norm techniques by enforcing the spatial focality of the reconstructions [Ou et al., 2009; Schmidt et al., 1999]. In addition to a modification of the diagonal elements of **R** (i.e., a modification of its autocovariance), the introduction of off-diagonal elements also results in sparser estimates and can circumvent the tendency of the pseudoinverse to posit adjacent or interleaved current elements of opposite polarity to precisely match the observed field or potential distribution [Grave de Peralta et al., 2004; Pascual-Marqui et al., 1994]. In the general framework of Bayesian models, these parameters can be inferred from the data [Friston et al., 2008; Mattout et al., 2006; Trujillo-Barreto et al., 2004; Wipf and Nagarajan, 2009].

In this context, the development of high spatial resolution functional imaging of the blood oxygenation level-dependent (BOLD) signal opens new opportunities to introduce functional priors into the inverse procedure. In particular, several authors have used the activations obtained from functional magnetic resonance imaging (fMRI) to improve EEG/MEG reconstructions. George et al. [1995] for example, used the BOLD responses obtained from the same stimuli to set the diagonal elements of **R** to non-zero values at source locations where the BOLD activations were above a given threshold. However, although both the BOLD [Logothetis, 2008] and the EEG/MEG [Hämäläinen et al., 1993] signals have good correlations with synaptic activity, the underlying processes have different origins [Nunez and Silberstein, 2000] and the presence of errors in the fMRI reconstructions (false-positive as well as false-negative) can introduce bias in the model [Vanni et al., 2004]. Several studies have proposed to weaken these effects by imposing a partial fMRI constraint [Ahlfors and Simpson, 2004; Dale et al., 2000; Liu et al., 1998, 2002]. More recently, Liu and He [2008] estimated the cortical activity using an adaptive Wiener filter in which the covariance matrix **R** was estimated by assuming that the time integral of each source variance was related to its BOLD-fMRI response [see also Liu et al., 2009 for application to visual data]. In Yoshioka et al., [2008], the prior on the source covariance was considered as a random variable whose parameters depended on the fMRI activity but could be updated according to the observed EEG/MEG data using hierarchical Bayesian estimation [see also Sato et al., 2004]. Finally, Ou et al. [2010] applied a reweighted minimum-norm algorithm where the source weights were estimated from both the EEG/MEG and fMRI data. While these different techniques have proven to be accurate on both synthetic and real data, their use is however complicated at the scale of group studies as they require a new fMRI acquisition every time a change is introduced in the stimulus.

FMRI data can be used in a different way to serve as a source constraint. Hagler et al. [2009] used retinotopic maps obtained from fMRI to prelocalize the portions of visual areas V1, V2, and V3 associated to specific locations in the visual field. These areas allowed the definition of a constrained EEG/MEG forward model that is theoretically usable to estimate current density in the three predefined visual areas for any stimulation in the prespecified parts of the visual field.

Here, we take a similar but more general approach. We present a new technique based on a functional area constrained estimator (FACE) that defines the source distribution correlation matrix using cortical regions that are determined once for any individual participant. These regions consist either of the topographic maps of the sensory surfaces onto cortex or functional localizers that can be used to define cortical areas on the basis of stimulus selectivity. The associated constraints are independent of any given experimental protocol and thus can be reused. We illustrate the FACE approach in the specific context of the visual system which contains several retinotopic maps of the visual field as well as several areas with distinct functional properties, all of which can be obtained with good precision using fMRI.

In the following, we first describe the different source models derived from the correlation properties of the predefined visual areas and explain how to introduce them in a minimum-norm inverse procedure. We then evaluate model performance using multiple EEG Monte-Carlo simulations. We use a real EEG data set to demonstrate the ability of our approach to localize the cortical generators responding to horizontal disparity. We show that our approach can be successfully introduced into other inversion frameworks, including a depth-weighted minimum-norm [Lin et al., 2006], a LORETA [Pascual-Marqui et al., 1994], and a MSP [Friston et al., 2008] inverses. Finally, we discuss the utility of inter-area correlations and potential errors associated with the use of distributed approaches.

METHODS

In this section, we first provide the notation and definitions classically used in the distributed source estimation problem and describe some of the priors presented previously in the literature. We then propose models that use the functional properties of the visual system to define the spatial correlations in the source current distribution.

Background

If we assume that the n cortical sources are localized on the cortical manifold with orientations normal to the local surface, the EEG/MEG forward model of m instantaneous data at time t can be written [Baillet et al., 2001]:

$$\boldsymbol{M}(t) = \boldsymbol{G}\boldsymbol{J}(t) + \boldsymbol{\varepsilon}(t) \tag{1}$$

where $\boldsymbol{M}$ is a column vector containing the m measurements on the EEG or MEG sensor array at instant t; $\boldsymbol{J}$ is a

column vector of the n unknown source amplitudes of all elementary sources in the model with zero mean and a covariance matrix $\mathbf{R}$ (size $n \times n$); $\mathbf{G}$ (size $m \times n$) is the forward gain matrix sampled at the sensor array [Hallez et al., 2007; Mosher et al., 1999]; ε (size $m \times 1$) is an additive nuisance term with zero mean and a covariance matrix $\mathbf{C}$ (size $m \times m$). The under-determination associated with this linear system (i.e., $n >> m$) leads to an infinite number of solutions [Hämäläinen et al., 1993]. This issue can be addressed by adding a prior on the source distribution to constrain the problem. A classical approach considers the currents to be spatially smooth. The solution can then be estimated using the well-known class of minimum-norm inverse operators [Wang et al., 1992]:

$$\hat{J} = RG'\left(GRG' + \lambda^2 C\right)^{-1}M \tag{2}$$

where λ is a regularization parameter. The value of the regularization parameter can be fixed a priori or can be estimated using the L-curve or the generalized cross-validation approach [Babiloni et al., 2004].

Introduction of Priors for Source Distribution Estimation

In this article, we propose different approaches to introduce priors within the matrix $\mathbf{R}$. Historically, this matrix has been referred to as the "source covariance" matrix. However, as our priors will be equally applicable to both MEG and EEG signals, we prefer to use the term "correlation matrix" in the following, which implies a unitless matrix that is proportional to the covariance. Focussing on the visual system, we use predefined visual areas V1, V2, V3, V3A, V4, as well as the lateral occipital cortex (LOC) and the middle temporal area (MT) as source constraints. These regions are now routinely derived from specific stimulation of the visual field [Huk et al. 2002; Kourtzi and Kanwisher, 2000; Sereno et al., 1995; Wandell et al., 2007]; see the section "Definition of the visual regions of interest" for more information on their determination.

In the following, we will denote υa (for visual areas) as the set of regions-of-interest (ROIs) and $n_{υa}$ as the number of areas it contains (here, $n_{υa} = 7$). υa is uniquely defined for a given participant and is activated in part or in total in any visual stimulation experiment. As our correlation models aim to characterise the current density relationship within each of the visual areas, we also use the term $R_{υa_k}$ − $k \in [1;n_{υa}]$− to refer to the submatrix obtained from $\mathbf{R}$ and that gives the correlation between every pair of sources within the kth ROI. $R_{υa_k}$ is therefore a square matrix whose number of columns is equal to the number of elements embedded in area k.

The visual areas υa can constrain the source correlation matrix in two different ways: the first only considers the autocorrelation of the current distribution, while the second reinforces mutual activity in neighboring sources belonging to the same functional regions.

Estimator based on the autocorrelation (autocorrelated FACE)

In vision studies, the neuronal populations embedded in our predefined areas are more likely to be activated than are sources in non-visual areas. Mathematically, the penalty for sources in the associated cortical areas can be decreased by changing the diagonal elements in the $R_{υa_k}$ submatrices. This operation strengthens the values of their autocorrelation $R_{υa}(i,i)$ relative to the ones of the other sources in nonvisual areas:

$$R_{υa_k}(i,i) = \alpha, \tag{3}$$

where α is a scalar. A value of one restores the estimate to the classical minimum-norm uninformed solution, whereas an increasing value biases the source space to lie within the visual areas. In practice, we find that α should not be larger than 2 or 3 when sources may be present outside the predefined ROIs.

Estimator based on the correlation (FACE)

The off-diagonal elements of $\mathbf{R}$ can be used to introduce a correlation between sources. Well-known methods such as LORETA consider that neighboring sources are more likely to have simultaneous activations [Pascual-Marqui et al., 1994]. In the visual system, the horizontal connectivity of the neuronal populations embedded within each ROI and the existence of retinotopic maps implies that the activity within a given functional area is likely to be more correlated with itself (although some stimulus structures may lead to activity that does not obey this rule). As the EEG/MEG signals are related to the neuron spiking rate [Hämäläinen et al., 1993; Logothetis, 2008] and the spiking rates of neurons within the same cortical area are correlated [Cohen and Maunsell, 2009; Kenet et al., 2003; Lampl et al., 1999], the voltages coming from close sources belonging to the same area should be highly similar.

In practice, this increase in correlation can be modeled by changing the off-diagonal elements of the submatrices $R_{υa_k}$. For each pair $(i;j)$ of sources belonging to area $υa_k$, the value $R_{υa_k}(i;j)$ of their correlation can be modeled by a function $f(d_{ij})$ of the distance d_{ij} that separates them. If the values of the function are equal to zero for every distance d_{ij}, the model is uncorrelated. If they are always set to one, the model assumes a perfect correlation within the entirety of the ROI, which is comparable to fitting a single dipole to the area. In this context, a plausible choice for f is to use a neighborhood of order N on the cortical tessellation instead of the distance and to affiliate decreasing values to $R_{υa_k}(i; j)$ as the order of the distance between i and j goes up to a predefined value. We propose here to use the first
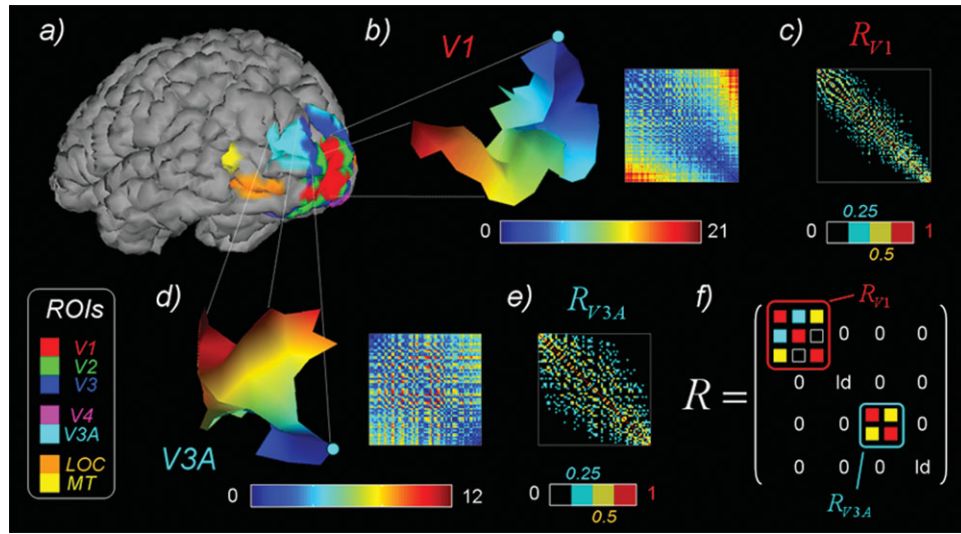
Figure 1.

Definition of the source distribution correlation matrix R using a prior on the neighborhood relationships within the ROIs. **(a)** Anatomical locations of the different visual ROIs defined using fMRI. **(b)** Illustration of the computation of the correlation sub-matrix corresponding to V1 and noted $R_{\upsilon 1}$. From the distances within the regions (one example is provided for the distance to a seed that is displayed in cyan), we derive the neighborhood matrices and obtain $R_{\upsilon 1}$ (panel **c**). Panels **(d)** and **(e)** illustrate the same process for area V3A. **(f)** At the end, these submatrices are incorporated in the matrix R that describes correlations within the complete source space. Id stands for the identity matrix.

and second order neighborhoods of each individual source within the visual ROIs.

$$R_{\upsilon a_k}(i,j)_{i \neq j} = \begin{cases} \alpha_1 & \text{if } j \in N_i(1), \\ \alpha_2 & \text{if } j \in N_i(2), \\ 0 & \text{otherwise,} \end{cases} \quad (4)$$

with $\alpha_2 \leq \alpha_1 \leq 1$. $N_i(1)$ and $N_i(2)$ are the two first order neighborhoods of source i respectively. The first order neighborhood of source i is defined by all the sources connected to it in the cortical mesh (see the "Simulation environment" section). Higher order neighborhoods are obtained by applying this rule recursively ($N_i(n + 1)$ contains the source directly connected to $N_i(i)$) that are not already affiliated to a lower rank neighborhood).

Different estimators can be derived from the pair $(\alpha_1;\alpha_2)$, depending on the strength of the correlation one wants to embed in the prior:

- Focal FACE: $(\alpha_1;\alpha_2)$ takes small values and defines a weak Markovian relation within each of the visual ROIs, which is equivalent to a small extent of the cortical current distributions of these regions. This assumption makes more sense in the case of a focal stimulation of the visual field.
- Extended FACE: $(\alpha_1;\alpha_2)$ takes higher values and is associated with extended stimulation where the main

part of the visual field is activated, as the stimulus itself will enforce correlated activity across a large area.

Estimator based on both the correlation and autocorrelation (combined FACE)

From these two types of priors, it is easy to derive a third one where the autocorrelation is increased for the visual areas and correlations are enforced between sources belonging to the same area and neighborhood. This is realized by combining (3) and (4).

Figure 1 illustrates the creation of the matrices $R_{\upsilon a_k}$ using this last type of prior with a model where the diagonal elements were set to 2 in the visual areas (leading to an autocorrelation two times larger) and the correlation parameters were chosen equal to 0.5 and 0.25 within the first and second order neighborhood of each visual source. From these submatrices, we define a new version of **R** that will be used to compute the current estimates (see panel f).

In practice, the full correlation matrix **R** that contains all the submatrices $R_{\upsilon a_k}$ can be very large when considering a realistic representation of the cortical surface (typically, about 20,000 sources are necessary). However, as our model does not consider the inter-area correlations, **R** is sparse and can thus be stored easily. Solving (2) involves a Cholesky decomposition of **R** and consequently of the

$R_{\upsilon a_k}$. As several choices may lead to non semi-definite matrices for certain visual areas, we possibly rewrite the concerned $R_{\upsilon a_k}$ from their eigenvalue decompositions by setting all their negative eigenvalues to 10^{-5}. This leads to a decomposable matrix whose global correlation properties remain unchanged.

RESULTS

In this section, we first present the performance of the different estimators using realistic EEG Monte-Carlo simulations and reconstructions from a classical L2-minimum-norm algorithm [see Eq. (2) in the "Methods" section]. Our main objective is to demonstrate that, under a given and fixed framework, our priors on the source covariance matrix **R** can improve the source estimates. We discuss their performance in different situations and evaluate the influence of both the number of active sources and their sizes. We then discuss the robustness of the models to misspecifications in the localization prior and their ability to reconstruct sources with different time courses. We also present real EEG measurement reconstructions obtained from a steady-state stereoscopic stimulation of the neuronal populations that respond to horizontal disparity modulation. We then demonstrate that the enhancements provided by our approach are not specific to the classical uninformed minimum-norm solution and are obtained for other inversion frameworks. Finally, we discuss the utility of introducing inter-area correlations and demonstrate that realistic levels of coregistration errors between the MRI and EEG coordinate systems do not affect the results.

Simulation Environment

Definition of the forward problem

Our simulation environment was derived from a real EEG acquisition set-up consisting of 128-sensor recordings performed on normal adult participants (HydroCell Sensor Nets, Electrical Geodesics, Eugene OR). As part of the source estimation procedure, Boundary Element Method (BEM) head-tissue conductivity models were derived from T1 and T2 weighted MRI scans of the individual participant (Siemens Trio 3T, 1 mm isotropic resolution). The FSL toolbox (http://www.fmrib.ox.ac.uk/fsl/index.html) was used to segment contiguous volume regions for the scalp, outer skull, inner skull, and the cortex and to convert these MRI volumes into inner skull, outer skull, and scalp surfaces [Smith, 2002]. The boundary element equations were computed from these surfaces using the MNE Suite [Hämäläinen and Sarvas, 1989]. The FreeSurfer software package (http://surfer.nmr.mgh.harvard.edu) was used to perform gray and white matter segmentation and a mid-gray cortical surface extraction for use with the cortically constrained minimum norm inverse. The FreeSurfer package extracts both gray/white and gray/cere-brospinal fluid (CSF) boundaries, but these surfaces can have different surface orientations. In particular, the gray/white boundary has sharp gyri (the curvature changes rapidly) and smooth sulci (slowly changing surface curvature), while the gray/CSF boundary is the inverse, with smooth gyri and sharp sulci. To avoid these discontinuities, we generated a surface tessellation partway between these two boundaries that has gyri and sulci with approximately equal curvature. Sources were constrained to lie on this surface with their orientation constrained to the local surface normal. A Polhemus FASTRAK system is used to record the 128 electrode positions (128 channels), fiducial landmarks (nasion, left, and right tragus), and several hundred points distributed around the scalp and face surface. Coregistration of the electrode positions to the MRI head surface was performed using a least squares fitting routine in Matlab. The algorithm starts by first, using the three digitized fiducial points (nasion, left, and right ears) along with their visible locations on the anatomical MRI to generate an initial alignment to the MRI coordinate frame. From this initial estimate, we find a rigid body transform that minimizes a cost function that combines the distance from digitized scalp points and the digitized electrode positions. For the digitized scalp points, we minimize the sum square distance to the MR defined scalp. However, our electrodes are digitized at locations off the scalp due to the height of the electrode holders. For this reason, we do not want to strictly minimize their distance to the scalp, but want to find a fit that ensures all electrodes are equidistant from the scalp. Therefore, for the electrodes we use an error term that minimizes the variance of the electrode distance to the scalp. This approach provides an accurate coregistration whose mislocalization error typically ranges below 3 mm.

Definition of the visual areas

fMRI scans were collected on a 3T Siemens TIM Trio scanner. Data were acquired with a custom whole-head 2-channel coil or a 2-channel posterior head surface coil and a spiral K-space sampling pulse sequence. The general procedures for these scans (head stabilization, visual display system, etc) are standard and have been described in detail elsewhere [Brewer et al., 2005]. Retinotopic field mapping produced ROIs by manual definition of visual cortical areas V1, V2v, V2d, V3v, V3d, V3A, and V4 in each hemisphere [Tootell and Hadjikhani, 2001; Wade et al., 2002]. ROIs corresponding to hMT+ were identified using low contrast motion stimuli similar to those described by Huk [2002].

The lateral occipital complex (LOC) was defined using a block-design fMRI localizer scan. During this scan, the observers viewed blocks of images depicting common objects (18s/block) alternating with blocks containing scrambled versions of the same objects. The stimuli were those used in a previous study [Kourtzi and Kanwisher, 2000]. The regions activated by these scans included an

area lying between the V1/V2/V3 foveal confluence and hMT+ that we identified as LOC. This definition covers almost all regions (e.g., V4d, LOC, and LOp) that have previously been identified as lying within object-responsive LOC [Kourtzi and Kanwisher, 2000; Tootell and Hadjikhani, 2001].

Monte-Carlo Experiments

Different numerical Monte-Carlo simulations were performed with the anatomy and functional areas from one subject to evaluate the effects of the number and sizes of active regions and misspecification of the prior on localization accuracy:

1. We were first interested in the ability of FACE to characterize distributions of different complexities. We generated 600 simulated trials of simultaneous activation of clusters of elementary sources contained in 1, 2, or 4 randomly chosen visual areas (200 trials for each class of visual area number, one new set of areas for each trial). The spatial extents of these clusters were scaled to activate equal fractions of each area and this fraction was randomly varied on each trial to be between 10 and 100% of the corresponding visual area.

2. We were then interested in the effects of the extent of the activated clusters. We generated another 600 simulations in which their sizes varied between 10, 50, and 100% of the full surface of the ROI they belonged to (200 trials for each size). The number of simultaneous activations was randomly chosen between one and four.

3. In a last set of simulations, we confronted our approaches with errors in the localization prior by adding activity outside the predefined visual areas. We generated 1,000 trials that simulated 4 clusters of elementary sources whose extents randomly varied between 10 and 100%. Within this set, the 200 first simulations were obtained by randomly defining four clusters outside the visual areas (in this case, the reference area to control the extent of the cluster was the average surface area of the visual ROIs). In the three next sets, the ratio between clusters outside the visual areas (which are not activated a priori) and clusters within the visual areas (which thus respect the prior) was increased and equal, respectively, to 1/3, 2/2, and 3/1. The last 200 simulations corresponded to four clusters within randomly chosen visual areas.

In all simulations, the sources localized within the activated clusters had a sine wave response with a zero phase (four oscillations, 360 time samples). The amplitude within each of these clusters was randomly chosen between 1 and 10 (important magnitude differences therefore existed between the amplitudes of the different clusters). The signals at the electrode level were generated using the matrix G obtained with the BEM model (see "Simulation environment" section). Independent and identically distributed (IID) Gaussian noise was added to all the EEG measurements corresponding to these datasets. The amplitude of the noise was chosen to obtain a signal-to-noise ratio (SNR) of 10. In this case, the SNR was defined as the ratio between the variance of the signal and the variance of the noise across the time.

Finally, we estimated the source distribution corresponding to the first maximum of the sine wave (i.e., if different time samples were used to define a SNR based on the noise variance across time, the reconstructed activity was only associated with one single time element). For each single simulation, this source distribution therefore consisted in one single vector with varying magnitudes in the different activated visual areas.

Evaluated Approaches

We reconstructed the source distributions for each simulation using different FACEs:

a. The first estimator was associated to an uninformed correlation matrix and was thus equivalent to the classical minimum-norm approach where $R = $ Id.

b. The second estimator (focal FACE) used a prior on the correlation within the visual ROIs with a small neighborhood of influence: 0.2 and 0.1 for the first and second order neighborhood coefficients (see the "Estimator based on the correlation" section). Its intrinsic definition assumes focal correlations of the cortical activations within each ROI (such as would occur with stimulation by small objects in the visual field).

c. The third estimator (extended FACE) was also based on the off-diagonal terms of the correlation matrices $R_{\upsilon a_k}$ but considered a wider Markovian correlation (0.6 and 0.4 for the first and second order, respectively). It was intended to model an extended internal-area correlation corresponding to a global stimulation of the visual field.

d. The fourth estimator (autocorrelated FACE) used only a prior on the autocorrelation (see the "Estimator based on the autocorrelation" section), assuming that its value was 2 times greater in the visual areas ($R_{\upsilon a_k} = 2 \times$ Id). The associated model does not embed off-diagonal terms and thus does not deal with intra-area correlations.

e. The last estimator (combined FACE) combined both the autocorrelations of the visual sources and their inter correlations (see the "Estimator based on both the variance and autocorrelation" section). The intra-area correlation prior corresponded to the one used for the autocorrelated FACE (i.e., a variance 2 times greater in the visual areas) and the correlation coefficients were chosen to correspond to an extent that was in between the ones described in the focal

and extended FACE (0.5 and 0.25 for the first and second orders correlation coefficients).

The results obtained from these different estimators allowed us to characterize the performance improvement obtained by adding information on the autocorrelation (when comparing the autocorrelated FACE to the minimum-norm), on the correlation (when comparing focal and extended FACEs to the minimum-norm or the combined FACE to the autocorrelated) or both (when comparing the combined FACE to the minimum-norm).

Evaluation Procedure

In this section, we describe the validation metrics used to estimate the detection accuracy of the different estimators in the Monte-Carlo simulations. As we aim to characterize the relative distribution of the currents and are less interested in their absolute value (i.e., we mainly want to be able to localize the cortical areas which are the more activated and to estimate their relative differences of amplitude), we used the normalized value of the current distributions. For a given vector J, this normalization J_{nor} was defined for each element i by dividing $J(i)$ by the maximum of the distribution in absolute intensity:

$$J_{nor}(i) = \frac{J(i)}{J_{max}}; \; J_{max} = \max_{k \in [1;n]}(|J(k)|), \qquad (5)$$

where n is the number of elements in J.

For each simulation set, we note J_{ref} the normalization of the current distribution used to generate the EEG recordings and J_{est} the normalization of the corresponding estimation at the peak of the time course using one of the estimators. E_{ref} and E_{est} are the energies of the corresponding sources in the cortical tessellation. They are obtained by computing the absolute values of the elements of J_{ref} and J_{est}.

Relative energy

This value is given by the ratio between the normalized energies contained in the estimation of the active sources and the global distribution:

$$RE = \frac{\sum\limits_{i \in \Theta_a} E_{est}(i)}{\sum\limits_{i \in [1;n]} E_{est}(i)}, \qquad (6)$$

where Θ_a denotes the set of all the active sources in J_{ref}. n is here equal to the number of sources in the cortical tessellation. The relative energy specifies the amount of energy that is recovered by our reconstructions. A perfect estimation should lead to a value of one.

Area under the ROC curve (AUC)

The receiver-operating curve (ROC) is an estimator of the detection accuracy [Cottereau et al., 2007; Metz, 1986]. It evaluates the ability of a reconstruction to present strongest activities only for sources that were activated in the simulation. The AUC quantifies how well the estimated current detects true sources and rejects false positives.

For a given simulation, let us note Θ the set of inactive sources in J_{ref}. Given a threshold β varying between 0 and 1, a source S_i is:

- A true positive (TP) if S_i is active (i.e., $i \in \Theta_a$) and $E_{est}(i) \; \beta$.
- A false positive (FP) if S_i is not active ($i \in \Theta$) and $E_{est}(i) \; \beta$.
- A true negative (TN) if S_i is not active and $E_{est}(i) \; \beta$.
- A false negative (FN) if S_i is active and $E_{est}(i) \; \beta$.

From these values, we can define the threshold-dependent values of the specificity S_p and the sensitivity S_e:

$$\begin{aligned} S_e(\beta) &= \frac{TP(\beta)}{TP(\beta)+FN(\beta)} \\ S_p(\beta) &= \frac{TN(\beta)}{TN(\beta)+FP(\beta)}. \end{aligned} \qquad (7)$$

ROC curves are then obtained by plotting $S_e(\beta)$ against $1 - S_p(\beta)$, which is a monotonically increasing function. The AUC is an index of the specificity-sensitivity compromise of the corresponding model. An AUC close to 1 means that the model separates the active and nonactive sets of sources well. However, in our simulations, the number of inactive sources is very much larger than the number of active sources (even in the largest sets where four full visual areas were used, the number of sources was only several hundred out of the 20,000 contained in the cortex tessellation). Because only a few percent of the sources are true positives, a trivial solution that estimates zero everywhere would have a high correct reject rate that leads to a biased estimation of the false positive rate. To circumvent this problem, Grova et al., [2006] defined reduced sets of sources that diminished the number of inactive sources taken under consideration. Using a similar approach, we define even stricter subsets where the number of inactive sources is strictly equal to the number of active ones:

- A set that includes the active sources in J_{ref} Θ_a and their card (Θ_a) closest neighbors (where card is an abbreviation for cardinality and characterizes the number of sources in a set). The associated ROC curve and AUC (AUC$_{close}$) quantify the focalization ability of the models by estimating their ability to separate between active and nonactive sources in the closest neighborhood of the activity.
- A set that includes the active sources Θ_a and the card(Θ_a) sources outside the neighborhood of Θa (i.e., outside the set used to define AUC$_{close}$) whose

activities are the highest. The associated AUC (AUC_{far}) quantify the ability of an estimator to discriminate between the real activated sources and the local maxima localized far from the simulated set.

The corresponding index of detection accuracy is then defined by:

$$\text{AUC} = \frac{1}{2}(\text{AUC}_{\text{close}} + \text{AUC}_{\text{far}}) \qquad (8)$$

Focalization error

The focalization error of a reconstruction is given by the ratio between the estimated and theoretical energies of the current within the simulated sources [Im et al., 2003]. Similarly, we can assess the ability of focalization by estimating the normalized mean-square error on the simulated sources used in our simulations:

$$\text{FE} = \frac{\sum\limits_{i \in \Theta_a} [J_{\text{est}}(i) - J_{\text{ref}}(i)]^2}{\sum\limits_{i \in \Theta_a} [J_{\text{ref}}(i)]^2}. \qquad (9)$$

This parameter indexes the quality of the estimation of the relative energies within the set Θ_a of activated sources.

Example

As an illustrative example, let us consider the case where two different clusters corresponding to area V4 in both the left and right hemispheres are active. Figure 2 presents the simulated activity and the associated reconstructions for different models.

The reconstruction obtained without any prior (uninformed) is classically smooth and spreads over the cortical surface, completely. It nevertheless coarsely identifies the simulated activity [see Hauk, 2004]. Note, however, that in this case, the estimator is at the chance level when discriminating between close sources as the red ROC curve (i.e., the one used to define the $\text{AUC}_{\text{close}}$ value) is similar to the axis $y = x$, which gives the chance level (this axe is emphasized in white). By adding information on the correlation within each visual areas (focal and extended FACEs), we greatly reduce the number of false alarms and improve the reconstructions according to the relative energy, the AUC and the error of focalization. Interestingly, the estimator based on an extended correlation (extended FACE) is better in this case where the full V4 areas have been simulated. The autocorrelated FACE increases the relative energy compared to the minimum-norm reconstruction but is similar in terms of the AUC and the error of focalization. This issue disappears when a correlation prior is added (combined FACE).

Influence of the Number of Sources

We are now interested in the influence of the number of sources on the performance of the different estimators. Figure 3 presents the relative energy; AUC and error of focalization obtained from the Monte-Carlo simulations for 1, 2, and 4 activated visual areas, respectively (see the "Monte-Carlo experiments" section).

In the following, the differences between distributions were verified using a nonparametric test (Kolmogorov-Smirnov). For purposes of clarity in the figures, the statistical differences are not displayed but are described below.

The performance obtained with the uninformed minimum-norm is consistent with what is expected for a L2 solution of focal activations. The relative energy is low and the error of focalization and the AUC are good even when four different clusters of sources are simultaneously activated. The results show that the two estimators using the correlation (focal and extended FACEs) outperform the uninformed approach for each of the criteria computed.

These observations were statistically different and the highest of the corresponding P-values was lower than 0.001 ($P < 0.001$). We can also note that the performance of these estimators is less affected by the increase in the number of sources. The estimator using only the autocorrelation of the sources (autocorrelated FACE) increases the relative energy and the area under the curve in comparison to the uninformed minimum-norm ($P < 0.05$) but does not change the error of focalization. The ability of the associated inverse procedure to discriminate between the different ROI activations is not enhanced by a hypothesis on only the autocorrelation. However, when associated with correlation information (combined FACE), the error of focalization decreased to reach the performances obtained with focal and extended FACEs. This last estimator outperforms the minimum-norm and the autocorrelated FACE on the AUC and error of focalization ($P < 0.005$) and the minimum-norm in terms of relative energy ($P < 0.001$).

Influence of Source Size

This section presents the performance of the estimator using different size of activations in the Monte-Carlo simulations (see the "Monte-Carlo experiments" section). Figure 4 displays the boxplots we obtained. Once again, we observe that the two estimators using the prior on the correlation (i.e., focal and extended FACEs) perform better than the classical uninformed minimum-norm ($P < 0.01$, Kolmogorov-Smirnov test). The autocorrelated FACE also leads to better relative energy, AUC ($P < 0.01$) and equivalent error of focalization. When the correlation coefficients are added (combined FACE), the estimation is improved for all criteria ($P < 0.01$) in comparison to both the uninformed minimum-norm and autocorrelated FACE and provides a better relative energy than focal and extended FACEs for extent equal to 100% ($P < 0.05$). Not surprisingly, focal FACE has a better error of focalization than extended FACE for small
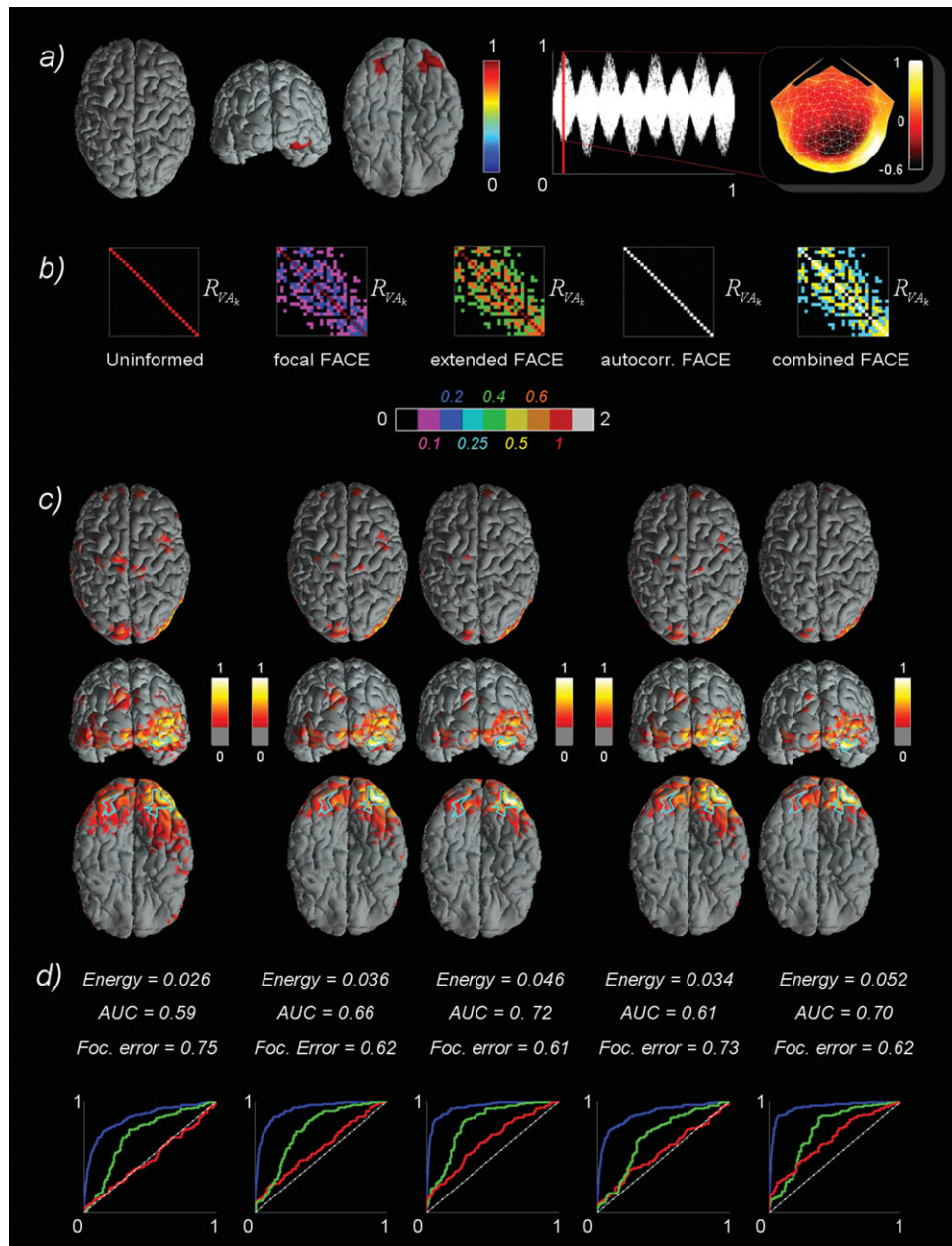
Figure 2.

Performance of the different estimators when area V4 is fully activated in both the left and right hemispheres. (**a**) Spatial localization of the activated sources (top, back, and bottom views of the corresponding cortex are displayed) and corresponding EEG time courses (in normalized units). The reconstructions are the corresponding normalized amplitude (in absolute value) is emphasized by the topographical display on the right, performed at the first maximum of the signal. (**b**) The matrices $R_{\upsilon a_k}$ associated to the visual areas inner-correlations for the different models. (**c**) Amplitudes (in absolute value) of the associated reconstructions (dorsal, back, and ventral views). The activities were normalized and thresholded at 20% of the maximum. The contours of the simulated areas are displayed in cyan to allow a better visualization of the reconstruction characteristics. (**d**) Evaluation parameters corresponding to this simulation and associated ROC curves. The curves obtained from the close set leading to the AUC_{close} values (see the "Evaluation procedure" section) are displayed in red. Those corresponding to AUC_{far} are displayed in green. We also display in blue the curve obtained from the full set of reconstructed sources. The white lines ($y = x$) are representative of what would be a ROC curve at the chance level.
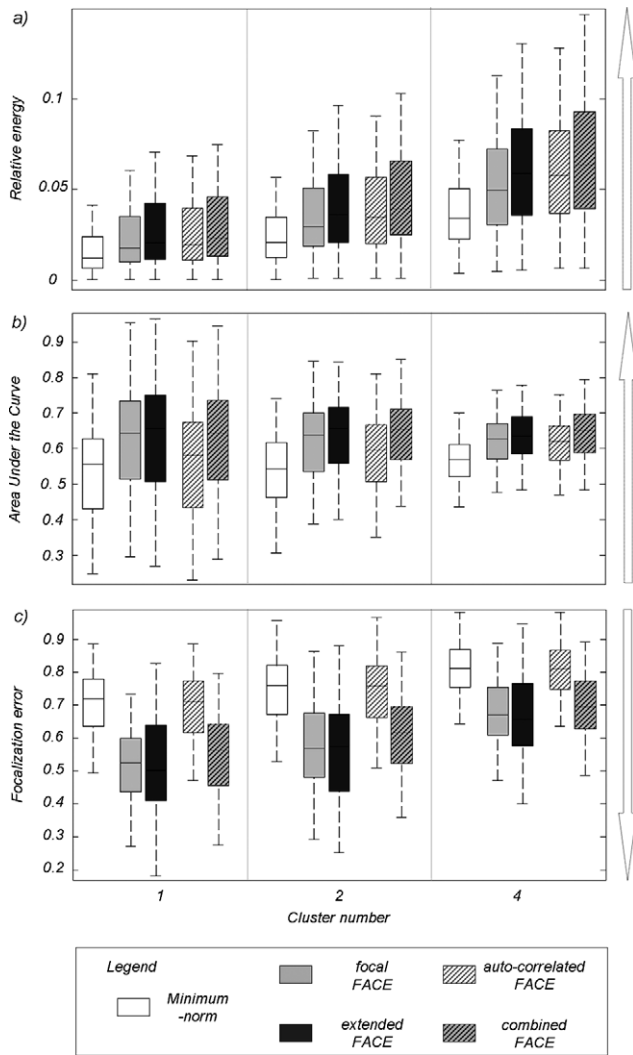
Figure 3.

Performance of the different estimators according to the number of activated visual areas. The boxplots show the different values for the first quartile, median, last quartile, and the extreme datum points from the Monte-Carlo samples. The arrows indicate the direction of the increase in performance. (**a**) Relative energy. (**b**) Area under the curve. (**c**) Focalization error.

patches ($P < 0.01$) whereas extended FACE outperforms it in terms of AUC and relative energy when 100% of the simulated clusters are activated ($P < 0.005$ and $P < 0.001$, respectively). It follows that the more veridical the prior is on the spatial correlation within the predefined areas, the more accurate the source distribution estimation.

Robustness of the Models to Misspecifications in the Prior

In this section, we evaluate the robustness of different estimators to misspecifications in the prior compared to

the classical uninformed minimum-norm reconstruction. For clarity in the display of the results, instead of using both the focal and extended FACEs, we defined a model with a medium intra-area correlation (0.5 and 0.25 for the first and second order neighborhood coefficients respectively) that is denoted as "medium FACE."

We simulated four regions of varying sizes within and/or outside the visual ROIs in five separate sets of data that differed in the fit of the prior: a fit of 25% corresponds to one cluster in the visual areas and three in the other part of the cortical surface (see the "Monte-Carlo experiments" section for a full description of the simulated data) while a fit of 0% corresponds to four clusters outside the visual areas (a fit of 100% is therefore associated with four clusters within four different visual areas).

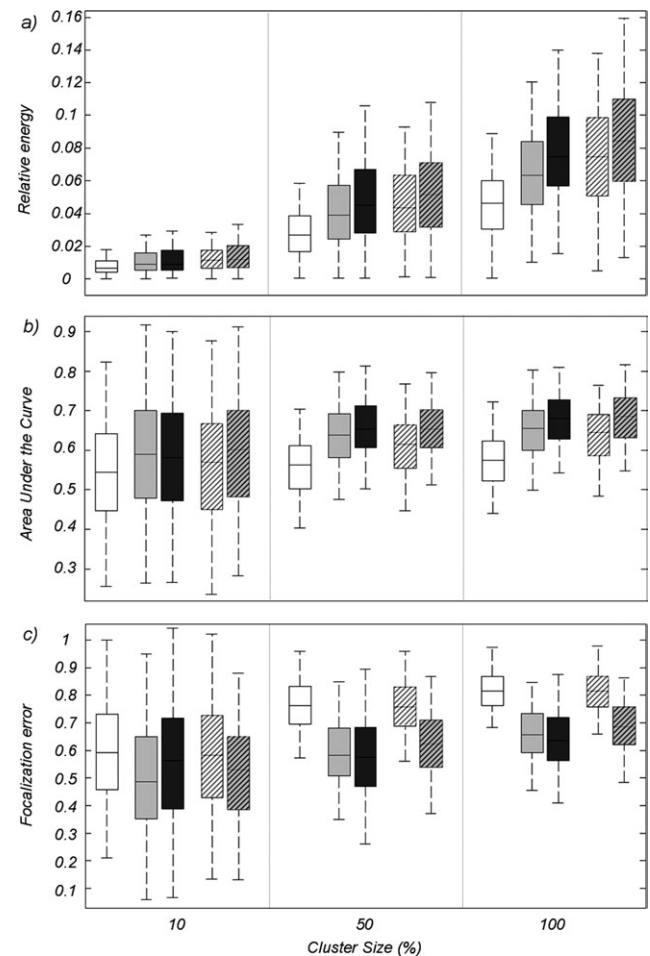Figure 5 presents the results we obtained in terms of the increase of performance from the corresponding

Figure 4.

Performance of the estimators for different sizes of activation. See Figure 3 for the definition of the boxes and estimators. (**a**) Relative energy. (**B**) Area under the curve (AUC). (**c**) Focalization error.
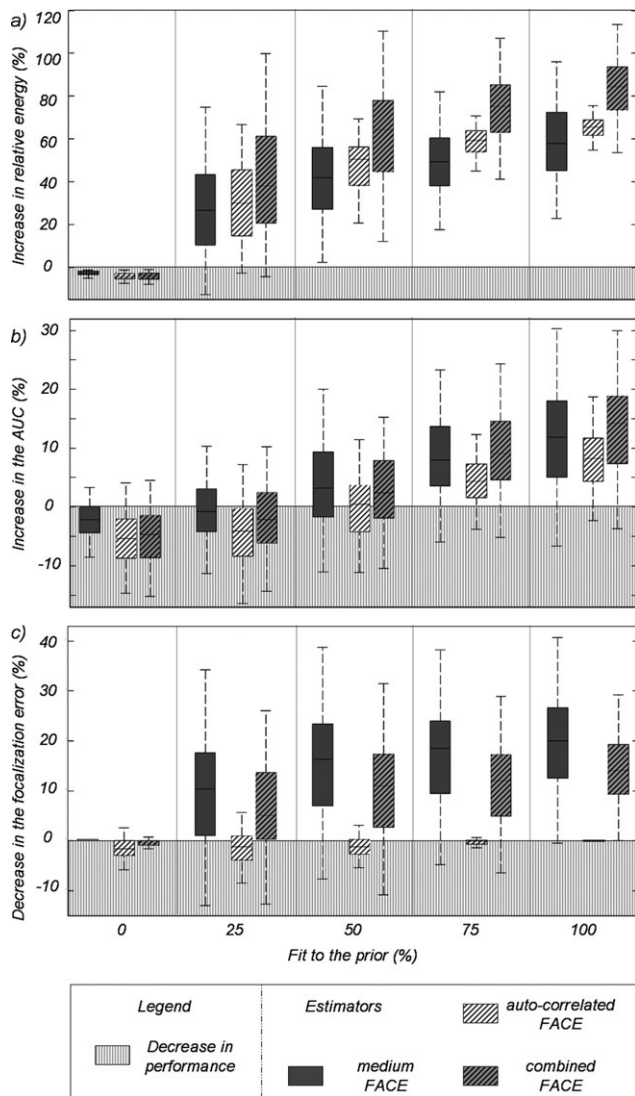
Figure 5.
Robustness of the different estimators to misspecifications in the prior on the activity localizations. The performance of three estimators is compared to the corresponding uninformed minimum-norm estimations when four regions were activated in the simulations. The fit of the prior gives the per cent of the four regions that were localized within the visual areas. The zones where the different priors penalize the reconstruction (i.e., where the increase is negative) have been emphasized. (**a**) Increase of the relative energy. (**b**) Increase of the AUC. (**c**) Increase of the focalization error.

uninformed minimum-norm estimates (an increase of performance is here characterized by an improvement of the relative energy and AUC and a diminution of the error of focalization). The zones associated with decreases of performance in the reconstruction have been emphasized by a barred box. The reference levels (associated to an increase

of 0%), which correspond here to the average performance of the minimum-norm estimates, were 0.027, 72.6, and 0.78 for the relative energy, the AUC and the focalization error respectively. As the minimum-norm is uninformed by definition, these values were equivalent across the subsets of simulation corresponding to the different fit of the prior.

We observe that our different estimators show weaker or equal performance when the prior is totally inappropriate (0%). However, as soon as the fit of the prior reaches 25%, the two models including an intra-area correlation prior (medium and combined FACEs) outperform the uninformed approach ($P < 0.005$, Kolmogorov-Smirnov test) for both the relative energy and the error of focalization. Their AUC values become statistically greater at 50% ($P < 0.05$). The estimator based only on the autocorrelation (autocorrelated FACE) also produces better relative energy when 25% or more of the activated sources are localized within the visual areas. The AUC was better when 75 or 100% of the sources respected the prior. However, its error of focalization suffers from the misspecifications in the prior and is always weaker or equal than the classical minimum-norm performances. In addition to this figure, Table I provides the proportion of AUC values that were informative (i.e., that were greater than 0.5 and thus superior to the chance level).

We can observe that, as far as the fit to our hypothesis is mainly respected, the reconstructions are above the chance level even for the restricted subsets of the data that we define to compute the AUC values (see the "Evaluation procedure" section).

Estimation Across Time

Time-course reconstructions from different cortical regions may be a difficult problem when their phase values or wave-shapes are different. Indeed, cross talk between the activated sources can lead to inappropriate estimates of the variance and therefore inaccurate reconstructions. As all the simulations described above only dealt with one single time-element (see the "Monte-Carlo experiments" section), we demonstrate in this section that our approach also outperforms uninformed inverses when estimating time-courses over a full time-window. We ran 200 new simulations where each activated cluster followed a sine wave (with four oscillations and 360 time samples as described in the "Monte-Carlo experiments" section). Each cluster had a randomly chosen phase (picked between 0 and 360°). The number of activated clusters

TABLE I. Proportion of AUC values above the chance level for the different values of the fit to the prior

FACE/Fit	0%	25%	50%	75%	100%
Medium	63%	68%	72%	84%	92%
Auto-cor	64%	63%	65.5%	72%	91%
Combined	70.5%	70%	72.5%	82.5%	94.5%

varied between 1 and 4. Their sizes were randomly picked between 10 and 100% of their own functional ROI and their amplitudes varied between 1 and 10. The noise level was defined as before to obtain an SNR of 10. We evaluated the accuracy of the reconstructions over all the time points using the metrics described in the "Evaluation procedure" section (i.e., the relative energy, the AUC and the focalization error). These metrics require knowledge of the active and inactive sets of sources in order for them to be computed. As a cluster with a varying time course may sometimes be inactive, for each time point, we considered as active the set of sources whose simulated absolute amplitudes were above 10% of the maximum value over the full time-window. In the following, we present the averaged values of the metrics across all the time points. In addition, we also computed the average correlation over the full time-window between each simulated source and its associated estimate.

We discuss here the performance obtained from the uninformed minimum-norm and three different versions of FACE: an autocorrelated, a medium and a combined FACEs (as in the "Robustness of the models to misspecifications in the prior" section).

The values obtained for the relative energy, the AUC and the focalization error are displayed in Supporting Information (see Fig. S1). The correlation values are given in Figure 6.

For the correlation values, the inverses with an intra-area prior (i.e., medium and combined FACEs) outperformed the minimum-norm ($P < 0.001$ for the two comparisons at the Kolmogorov-Smirnov test). Improved performance was also observed for each of the other metrics ($P < 0.001$, see Supporting Information Fig. 1). The autocorrelated approach outperforms the minimum-norm for the relative energy ($P < 0.001$) and the AUC ($P < 0.01$). These results demonstrate that the improved estimates obtained in our single time-point simulations also occur when estimating time-courses from clusters with different phase lags.

Illustration on a Real Dataset

It has been known for almost two centuries that horizontal binocular disparity produces the perception of depth [Wheatstone, 1838]. The last 15 years have seen tremendous growth in the number of articles exploring the physiological basis of depth from disparity [see Parker, 2007 for a review]. However, these studies have mainly focused on responses from individual neurons, rather than on population-level neural activities related to disparity. With the recent increases of spatial resolution in brain imaging, fMRI, but also EEG or MEG, are now good candidates to localize the cortical origins of these global activities.

In the following, we localized the neural sources encoding horizontal disparities with our models to demonstrate
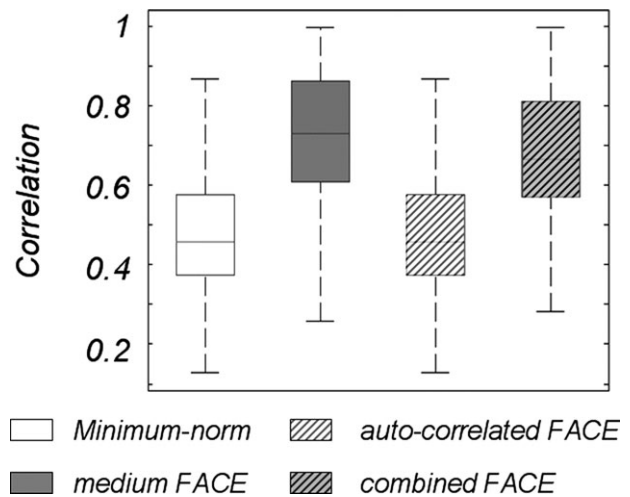

Figure 6.

Average correlation between the activated sources in the simulation and their associated reconstructions over a full time-window (200 simulations). Phase values were randomly chosen for each activated cluster. Four estimators are displayed: an uninformed minimum-norm, an autocorrelated, a medium, and a combined FACEs.

the improvements that can be obtained using functionally defined priors. Using dense dynamic random dot patterns, we modulated a disparity-defined central disk (5° diameter) at 2 Hz across the plane specified by a static annulus (12° diameter) presented at zero disparity. The disk was first periodically presented at 4 minutes of arc back from the surround (uncrossed disparity) for 250 ms and then at 4 minutes of arc in front of it (crossed disparity) for 250 ms. We recorded 25 trials of 10 seconds (leading to $25 \times 2 \times 10 = 500$ repetitions of the whole cycle) from six different participants using the high-density EEG system described in the "Simulation environment" section. The participants all had normal or corrected to normal vision. Their informed consent was obtained prior to experimentation under a protocol that was approved by the institutional review board of the Smith-Kettlewell Eye Research Institute. Their cortical surfaces and associated visual ROIs were defined using the procedure described in the see the "Simulation environment" section.

In the specific case of this experiment, which used steady-state stimulation, the frequency properties of the signals are known. It explains why here, rather than localizing the cortical source distributions associated with every single time instant and then looking at the amplitude distribution at one of its maximum (as in a event-related potential experiment), we used our prior knowledge of the stimulus frequency to perform the analysis in the frequency-domain. This approach has high signal to noise ratio [Cottereau et al., 2011a; Regan, 1989; Vialatte et al., 2010] and has been used in recent EEG studies from our group [Ales and Norcia, 2009; Appelbaum et al., 2006;

Cottereau et al., 2011b]. In this context, we were mainly interested in the reconstruction of the complex-valued Fourier coefficients corresponding to the second harmonic of the stimulation (i.e., 4 Hz). Note that as our model is linear, this is equivalent to reconstructing time-point after time-point and then computing the Fourier coefficient on each individual source. This amplitude in the source space is associated with population responses that are similar for crossed and uncrossed disparities and transitions between them.

Figure 7 presents the activity obtained using the uninformed minimum-norm and a combined FACE. This model assumed an autocorrelation twice as large within the visual areas and a second-order neighborhood correlation with 0.5 and 0.25 for the first and second parameters, respectively. The reconstructions obtained from these two different estimators are presented on the left and the right, respectively, for three subjects (see Supporting Information Fig. 2 for the three other subjects and Supporting Information Fig. 3 for a display of the times courses in four different visual areas averaged across subjects).

When looking at the reconstructions provided by the minimum-norm approach, we can coarsely observe that the main cortical responses are coming from both the ventral and dorsal pathways in the visual system. However, it is difficult to identify specific visual areas that would be activated in all six participants. In addition to that, the activations, which should be equivalent in the two hemispheres as our stimulus was the same in the left and right visual fields, show strong hemispheric asymmetry for participants 1, 3, and 6. When adding the informed prior, one can see that the reconstructions on every participant become more symmetric according to the inter-hemispheric map. Three regions are mainly activated for all the six subjects: MT, V3A, and V4. Although MT is well known for its strong response to motion, it is also strongly involved in disparity processing [DeAngelis and Uka, 2003; DeAngelis et al., 1998]. V3A and V4 have also shown tuned responses to disparity in recent studies [Backus et al., 2001; Tsao et al., 2003; Umeda et al., 2007]. Altogether, these results suggest that the use of a model based on functionally defined prior may facilitate the analysis of EEG/MEG data obtained when stimulating the visual system.

Performance under different inversion frameworks

In all the sections above, the performance of our approach was evaluated by adding our priors to a minimum-norm inversion procedure. Here, we characterize the improvements provided by our method on three other inversion frameworks. In addition to the minimum-norm inverse and its associated combined FACE estimator, we defined:

- A weighted minimum-norm inverse with a depth-weighting [see Lin et al., 2006 for the details of the

algorithm]. The associated FACE inverse was obtained by decomposing the correlation matrix in two parts: one with the depth weights and the other containing the visual areas information (i.e., the R_{va_k}).
- A LORETA inverse [Pascual-Marqui et al., 1994], which was obtained from the SPM software (http://www.fil.ion.ucl.ac.uk/spm/software/spm8/) and its associated FACE inverse.
- A Multiple Sparse Prior Approach (MSP) where each source had compact support and was locally coherent. The parameters used were the default parameters of the SPM software as previously described in [Friston et al., 2008]. The corresponding FACE version was obtained by changing the correlation support of all the sources within the visual areas. For each of these sources, the new support was given by rr^t where r is the row corresponding to the source in the global correlation matrix $\mathbf{R}$.

To characterize the improvements brought by the FACE approach, we generated 200 new Monte-Carlo simulations. In these simulations, the numbers of activated clusters within the visual areas were randomly chosen between 1 and 4, the extensions of the activation were comprised between 10 and 100% of the visual areas and each cluster had a uniform amplitude randomly fixed between 1 and 10. The SNR was set to 10 (see the "Monte-Carlo experiments" section for the details). We estimated the source distributions with the different inverse procedures. Boxplots of the relative energies, AUC and focalization errors (see the "Evaluation procedure" section) obtained are displayed in Figure 8.

We can observe that on average, all the four approaches without any intra-visual area priors (white boxes) perform equivalently well: the MSP approach has slightly better relative energy, but worse focalization error when compared to the minimum-norm. The depth-weighted approach also proposes decreased focalization errors. However, when the prior is added (gray boxes with bars), all the algorithms show increased performance ($P < 0.0001$ in the Kolmogorov-Smirnov tests for all the comparisons except when comparing the focalization errors between LORETA and its FACE version where $P = 0.0018$). For LORETA and the MSP approaches, the FACE versions greatly enhance the AUC, with means growing from 0.56 to 0.77 and from 0.53 to 0.80, respectively. Altogether, these results demonstrate the utility of our approach for widely different reconstruction frameworks.

Beyond Local Interactions: Performance and Limitations of Inter-Area Correlation

Because of the retinotopic properties of some of the areas used in this study, one may be tempted to introduce correlations between sources in different functional areas that correspond to the same part of the visual field. This prior would directly enforce the coactivations of these
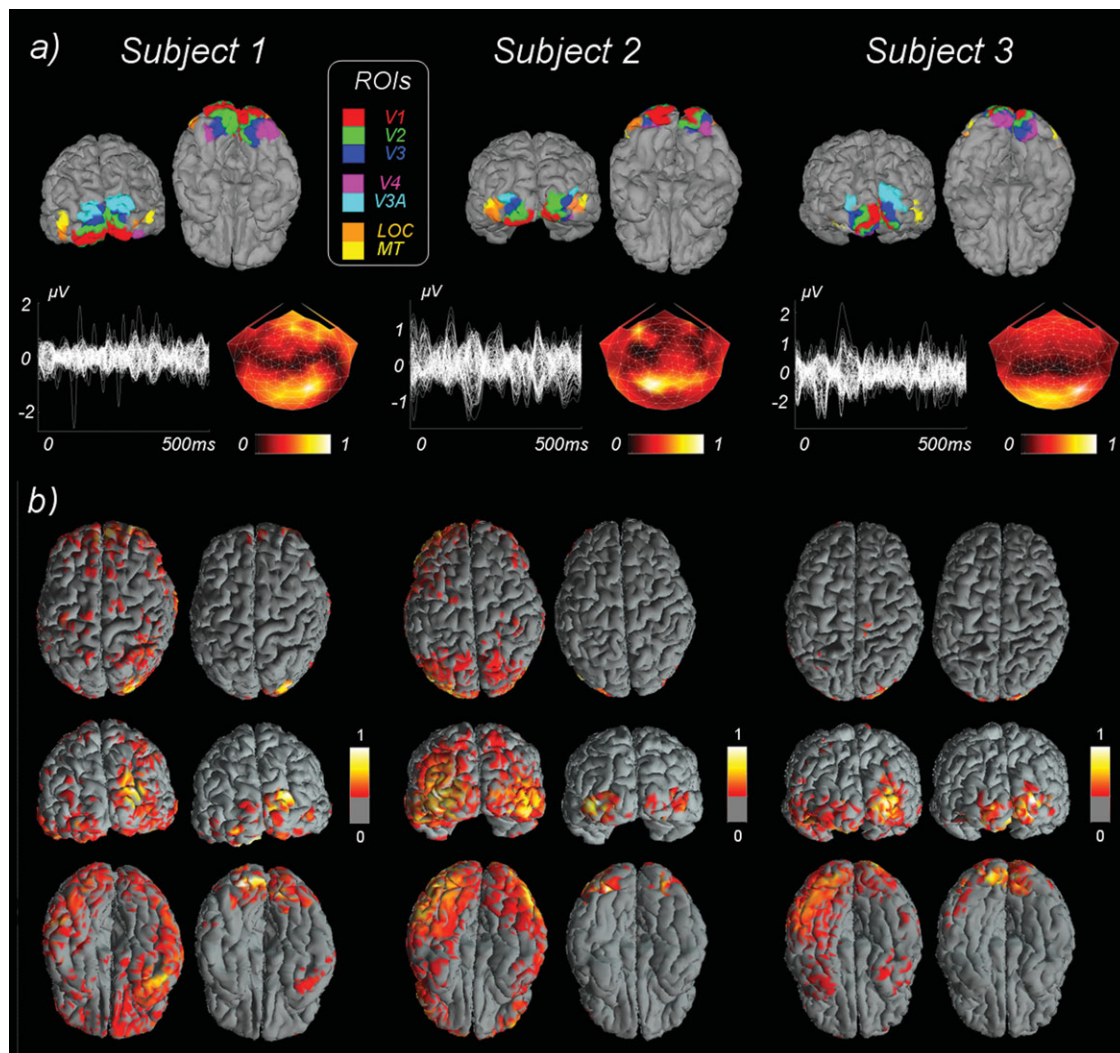
Figure 7.

Illustration of the method in a horizontal disparity evoked response study. (**a**) Data from three participants. The cortical surfaces (back and ventral views) are displayed with the different visual ROIs. The different plots in the sensor space present the time-averaged evoked potentials averaged for each of the 128 electrodes from 250 single trials and the associated normalized amplitudes at the second harmonic of stimulation. (**b**) Amplitude of the Fourier coefficient reconstruction obtained from the minimum-norm (left columns) and the combined FACE (right columns) are presented (dorsal, back, and ventral views from the top to the bottom). The estimations are normalized and thresholded at 20% of the maximal value.

sources at each time point and therefore produce a better estimation of the cortical activity. However, two possible limitations may be present:

• Two sources responding to the same part of the visual field may belong to functional areas whose properties are different. Therefore, one of these sources can respond to a stimulus displayed in its receptive field while the other does not. This situation can for example happen in the context of the disparity system (see the

"Illustration on a real dataset" section) where responses from the different retinotopic areas have distinct characteristics [Cottereau et al., 2011b; Parker et al., 2007].

• Two sources responding to the same part of the visual field may belong to functional areas whose dynamics are different [see e.g., Ales et al., 2010; Bullier et al., 2001].

In these two cases, a correlation term between the two sources may diminish the quality of the estimates, as the assumed model is incorrect. To illustrate the costs and
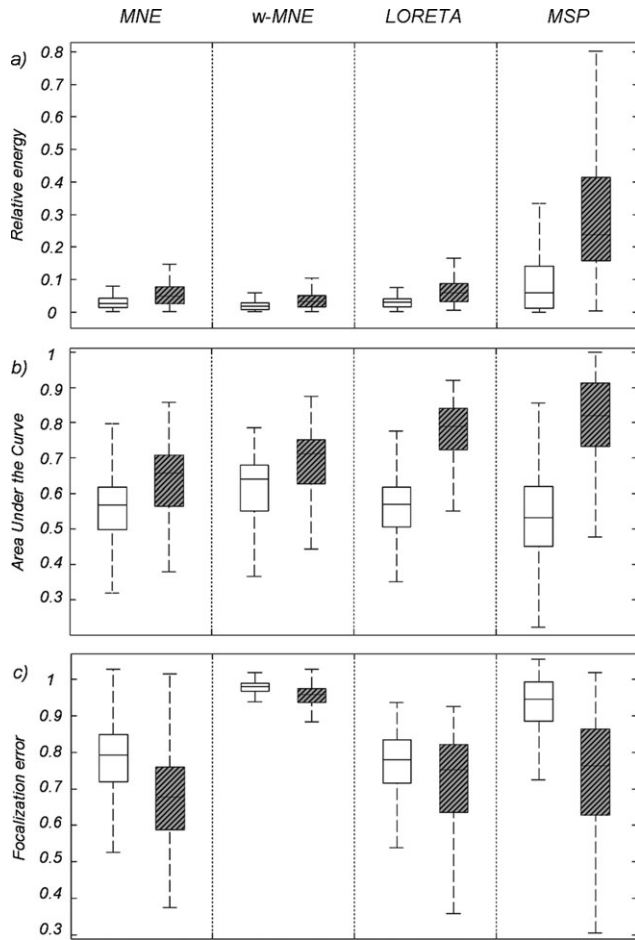
Figure 8.
Performance of different source estimation techniques with (gray boxes with bars) and without (white boxes) an intra-visual areas correlation prior. See Figure 3 for the definition of the boxes and estimators. (**a**) Relative energy. (**b**) Area under the curve (AUC). (**c**) Focalization error.

benefits of inter-areal correlations, we characterize here the performance of FACE approaches that include correlations between visual areas using new Monte-Carlo simulations. To compute the associated models, we extended the notion of intra-area neighborhood used in the "Estimator based on the correlation (FACE)" section to an inter-area neighborhood. Each source within a retinotopic area has now, in addition to its (intra-area) spatial neighborhood (which is used to define its local correlation), an (inter-area) retinotopic neighborhood. At the first order, this inter-area neighborhood is defined in each of the other retinotopic areas by the source whose coordinates in the visual field are the closer to the source. The second order neighborhood is defined by all the sources that are spatially connected to the first order sources and belong to the same area [see the "Estimator based on the correlation (FACE)" section and Fig. 9 for an illustration].

For each pair $(\upsilon a_{k1}/\upsilon a_{k2})$ of retinotopic areas, the associated correlation matrix $R_{\upsilon a_{k1}/\upsilon a k2}$ is then obtained using (4). If the global covariance matrix $\mathbf{G}$ now also contains off-diagonal elements associated with sources in different areas, it is still a sparse because the number of first and second order (intra and inter-area) neighbors of each source in a retinotopic area remains small.

We ran 200 simulations in which 2 to 4 clusters were activated. These clusters had the same retinotopic coordinates but were localized in different visual areas. Because in our study, LOC and hMT+ were defined using functional localizers and not from retinotopic mapping, only V1, V2, V3, V4, and V3A were used in this set. The extents of the clusters were set to 10% of their functional area (see the "Monte-Carlo experiments" section for more details). The noise level was defined as before to obtain an SNR of 10. The time courses were generated as in the "Estimation across time" section. For each simulation, we generated one version in which the different clusters had time courses with the same phase and one other where they had a random phase. A comparison between these two versions allowed us to determinate if different dynamics between regions may affect the performance in the specific case of a prior with inter-area correlations. The metrics used were those defined in the "Estimation across time" section.

Three FACE estimators were used; the first one was a focal FACE, which provides the best estimation for focal activations (see the "Influence of source size" section). The second one used an inter-area model where the values of
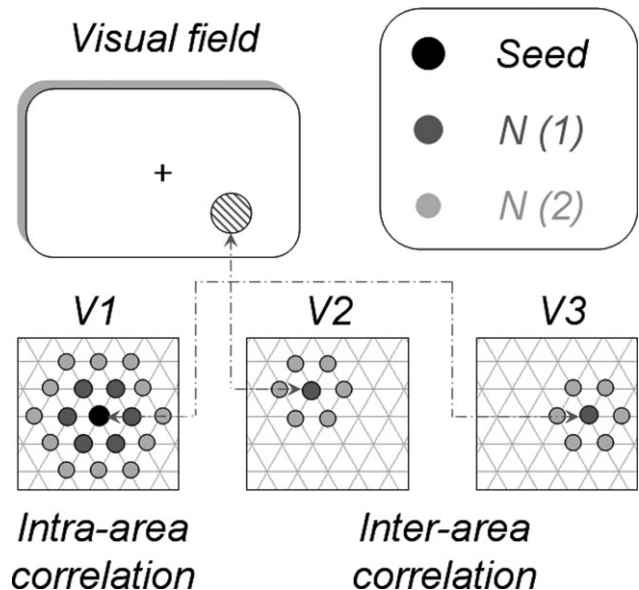

Figure 9.
Illustration of the definition of an inter-area neighborhood for one source in V1 and its first and second order retinotopic neighborhood in V2 and V3.
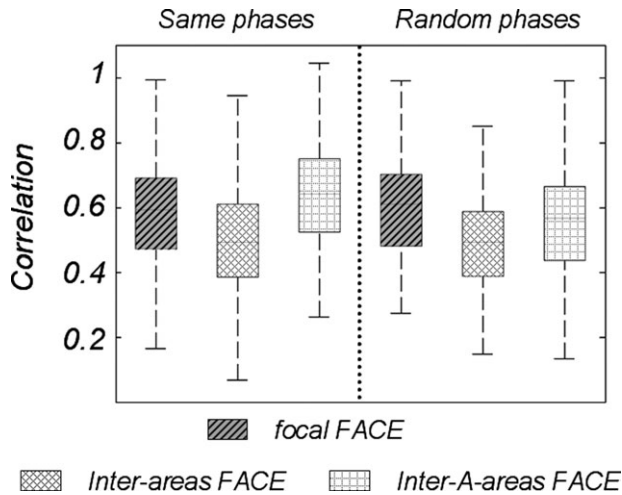
Figure 10.

Correlation values for inter-area correlation approaches. Three estimators are displayed: a combined, an inter-area correlated, and an inter-A-area FACEs.

the first order neighborhood (inter as well as intra-areas) were equal to 0.2 and those of the second order to 0.1. This inter-area FACE can therefore be seen as a focal FACE with additional off-diagonal elements for every couple of retinotopic areas. The last model, named inter-A-areas FACE (for inter-Activated-areas FACE), also had intra and inter-areas correlations with the same values (0.2 and 0.1) but for each simulated time-course, the inter-areas coefficients were only added in the visual areas that were activated (the plausibility of such a model is discussed in the end of this section).

Figure 10 displays the values obtained for the average correlation, the relative energy, the AUC and the focalization error are presented in Supporting Information Figure 4. For the two versions of the simulations (i.e., clusters in-phase and clusters with random phase), the correlations obtained with the inter-area FACE are worse that those with the combined FACE ($P < 0.001$, Kolmogorov-Smirnov test, see Fig. 10). The same trend is observed for the relative energy, AUC and focalization error (see Supporting Information Fig. 4). These weaker performances are not due to the way the inter-area correlation model is created as the inter-A-areas FACE, which is defined using the same approach, provides better correlations than the combined FACE when no phase lags are introduced ($P < 0.01$, see Fig. 10). This result illustrates that forcing the coactivation between retinotopically corresponding areas leads to degraded estimates when some of the areas are not responding to the stimulus. The correlations obtained with the inter-A-areas FACE are also diminished when a phase lag exists between the activated clusters ($P < 0.001$ when compared to the set without phase lag) and the results do not outperform those from the focal FACE approach anymore either (the mean values are 0.56 for the inter-A-areas

FACE and 0.59 for the focal FACE with a P-value of $P = 0.08$ for the comparison between the two sets). This trend is also observed for the other metrics (i.e., the relative energy, AUC and focalization error, see Supporting Information Fig. 4). This set of simulations demonstrates that phase lags between areas corrupt an estimate based on inter-area-correlations, even if the correlations are only introduced in the activated areas. In the end, the only case where inter-areal correlations improve the reconstruction is when the activated areas are known and their phases are identical (i.e., the inter-A-areas FACE with no phase lags). In the analysis of real data, the true sources, as well as their dynamics are unknown and the employment of such a model is therefore inadvisable. However, this approach can be valid for correlations between spatially separated sources from the same retinotopic area as in the left and the right visual fields. Introducing some correlation between sources associated with corresponding points in the two hemi-fields will improve the results if the two hemi-fields share similar dynamics.

Spatial Accuracy of Distributed Approaches

All the reconstruction techniques proposed here are based on distributed models that constrain the sources to be localized on the cortical manifold [Hämäläinen et al., 1993]. Their spatial accuracy may therefore be corrupted by the inherent errors in coregistering and reconciling the coordinate systems of MRI and the EEG measurement systems. To test if such registration errors have consequences for our estimates, we performed 200 Monte-Carlo simulations using the same parameters described in the "Performance under different inversion frameworks" section. Two inversion techniques were considered: the minimum-norm and a combined version of FACE. These inverses were either based on:

- The exact forward matrix used to create the simulations (as in the other sections of this study).
- A corrupted version of this forward matrix where the position of each of both the fiducials (nasion and peri-auricular points) and scalp surface points had Gaussian distributed noise with a standard deviation of 8.7 mm added. This value was chosen to range above others described in the literature as typical [see e.g., the 5 mm proposed in Schwartz et al., 1996]. The electrodes were then registered to the MRI coordinate using only the three fiducials. This procedure leads to electrode mis-registration errors up to 10 mm.
- A corrected version of this last version using all available points, as described in the "Definition of the forward problem" section. This procedure decreases the electrode mis-registration errors to below 2 mm.

The performance metrics computed were those used in the "Performance under different inversion frameworks"

section. The electrode and anatomical fiducial positions corresponding to the three models are displayed in Supporting Information Fig. 5a). The original values are in black while the corrupted and corrected versions are in red and green, respectively. The fiducials are given by the larger dots. Supporting Information Figure 5b presents a histogram of the errors in the electrode location (i.e., the distances to the original positions) before (red) and after (green) correction. With the correction algorithm, these errors are at or below 2 mm. Supporting Information Figure 5c–e displays the reconstruction accuracy obtained for the three different cases with the minimum-norm and a combined FACE. For the uninformed minimum-norm, the results are equivalent between the corrected version and the original one (i.e., no significant difference, Kolmogorov-Smirnov test). Interestingly, even the corrupted version leads to similar results (with the exception of the focalization error, which is significantly worse for the corrupted model when compared with the original one, $P <$ 0.047). This is consistent with observations made in other studies [Beltrachini et al, 2011; Wang and Gotman, 2001]. In addition, the use of a prior does not change this trend (no significant differences are observed between the different models for the FACE approach). However, for all the metrics used and all the models, the accuracy is again statistically better with FACE than with the minimum-norm ($P <$ 0.001). We conclude that potential errors in the coregistration between the coordinate systems of MRI and the EEG measurement system do not affect the results presented in this study.

Another issue with the distributed approaches is the use of a source-orientation constraint based on anatomy. In this study, we only considered a fixed-orientation constraint. Lin et al. [2006], showed that applying a loose-orientation constraint to a coarser model of about 7,500-dipolar sources improved by only a few millimetres the localization performances of a variety of distributed source imaging approaches with respect to image models with strict or totally free orientations. These improvements should be even smaller in our case where 20,000 sources were used. Note however that the implementation of a free-orientation version of our approach is straightforward.

DISCUSSION

In this study, we introduced a new method that uses functionally defined ROIs to constrain the solution of the EEG/MEG imaging problem in the context of stimulation of the visual system. The definition of the different source area is performed once for each participant and requires roughly 2 hours of fMRI scanning. As with older approaches, it allows the introduction of a prior on the autocorrelation of the current source distributions in the inverse procedure. However, as the ROIs are not defined using the same stimulus set but are instead fundamental aspects of the functional architecture of the visual system,

the inverse can be defined once for a given participant and reused for a wide range of experiments and we can also enforce the correlation between two neighbor sources embedded in the same visual area, based on their shared electrophysiological characteristics.

We proposed a general way of defining different models that can be derived from the intrinsic parameters of the stimulus, such as the size of the objects presented in the visual field, by modifying the values of the correlation coefficients. We used Monte-Carlo simulations to estimate the performance of our approach in the context of EEG recordings. However, this could also have been done with MEG data by simply replacing the forward matrices. The estimates presented in this study are all based on a distributed approach framework. As demonstrated and discussed in the "Spatial accuracy of distributed approaches" section, errors in the coregistration between the fMRI coordinate and the EEG measurement systems, as well as the use of a fixed orientation do not affect the results presented here.

Four different models were tested relative to the inverse solutions provided by the uninformed minimum-norm model. Importantly, the cortical distributions, which we derived were rather complicated as both the number of activated areas (from 1 to 4), their amplitudes (from 1 to 10 in n.u.) and their sizes (from 10 to 100%) were included in the model. The evaluation parameters were also very strict as only subsets of the cortical tessellation were taken into account (see the AUC definition in the "Evaluation procedure" section). We showed that every prior improve the reconstructions if the simulated areas are effectively localized in the visual areas and thus respect our hypothesis. This is true for different sizes and for different numbers of activated regions. Interestingly, the model based only on the autocorrelation of the predefined sources, even if better than the classical minimum-norm, does not outperform it, because of the focalization error. This illustrates that information on the true source localization does not increase the estimation of the relative amplitude differences between these sources. In contrast, the three models associated with a correlation prior show better results in this case. To test the impact of misspecifications in the model, we also evaluated the reconstructions when an increasing percent of sources were localized outside the visual areas. We showed that the three models using the correlation produce informative results (i.e., with an AUC mainly greater than 0.5), which are better than the uninformed minimum-norm reconstruction when at least 50% of the current spatial distribution is consistent with the localization hypothesis. In addition, we showed that the design of the prior can be optimized according to the size of the stimulus, small values of the coefficients being more adequate to focal presentation in the visual field while bigger values can be associated to bigger objects. We also provided evidence that the FACE approaches led to more accurate correlations with the true source time courses when the simulated clusters had different phases over a

full time-window (see the "Estimation across time" section).

We demonstrated the ability of our models to reconstruct real activities using EEG recording from six different subjects. We localized the neuronal populations responding to horizontal disparities using a steady-state analysis and emphasized the role of areas V3A, MT, and V4 in this context. These results are consistent across participants and agree with the recent single unit and fMRI literature. As we have noted previously [Appelbaum et al., 2006; Cottereau et al., 2011b], the availability of individually determined functional ROIs makes it possible to pool data across participants in a way that respects individual differences in the location, size and shape of different functional areas. While area V1 and V2 have a consistent relationship to the anatomical landmark of the calcarine sulcus [Hinds et al., 2009], higher-order areas, such as V3A show a large error of variation in their location. Nonetheless, ROI-based analysis can apportion activity appropriately based on the labeling of the cortex with respect to the retinotopic or functional maps.

The associated FACE procedure we presented for the main set of simulations and the analysis of the real data assumed a L2-minimum-norm uninformed procedure, this choice was mainly motivated by the fact that this method is widely used in the neuroscience community as emphasized by the increasing number of associated articles published in the last years [Busse et al., 2009; Cottereau et al. 2011a,b; Jerbi et al., 2007; Lefevre and Baillet, 2009; Schupp et al., 2007; Sergent et al., 2005]. However, our priors on the matrix **R** can be easily introduced into other reconstruction techniques if they include the correlation matrix of the cortical current distributions in the inverse procedure. By evaluating the performance of our approach on three other standard source estimators (i.e., a depth-weighted minimum-norm, a LORETA inverse and a Multiple Priors Sparse inverse, see the "Performances under different inversion frameworks" section), we demonstrated that our method provided enhanced estimations for all of them. We anticipate that every new algorithm could benefit from these types of prior.

We also discussed the possible use of inter-area correlations and emphasize potential issues in their direct implementation (see the "Beyond local interactions: performance and limitations of inter-area correlation" section). We nonetheless proposed specific conditions (e.g., increasing the correlation between sources belonging to the same area but lying in different hemispheres when a stimulus is symmetric across the two visual fields) under which such an approach can provide significant improvements. The integration of the corresponding priors in our estimation technique is straightforward and the proposed model always leads to a sparse representation of the correlation matrix.

Beyond the domain of vision, a method based on intra-area correlation may be successfully applied to other cognitive studies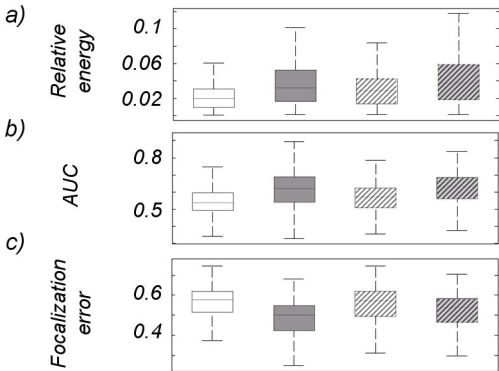 where the system is comprised of cortical fields that display systematic maps of sensory surfaces such as those that occur in the somatosensory and motor cortex [Penfield and Boldrey, 1937] or the auditory cortex [Di Salle, 2001] or that show particular functional specialization that can be mapped with localizer scans.
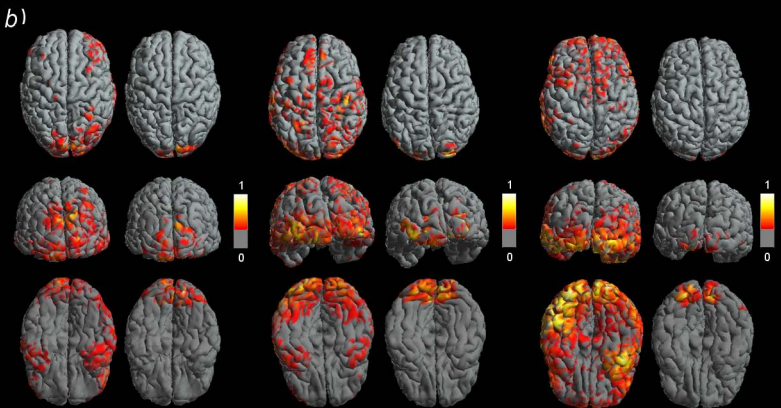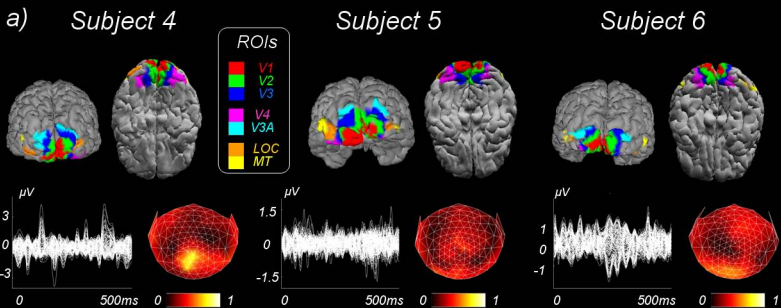
REFERENCES

Ahlfors S, Simpson G (2004): Geometrical interpretation of fMRI-guided MEG/EEG inverse estimates. Neuroimage 22:323–332.

Ales JM, Norcia AM (2009): Assessing direction-specific adaptation using the steady-state visual evoked potential: Results from EEG source imaging. J Vision 9:1–13.

Ales J, Carney T, Klein S (2010): The folding fingerprint of visual cortex reveals the timing of human V1 and V2. Neuroimage 49:2494–2502.

Appelbaum LG, Wade AR, Vildavski VY, Pettet MW, Norcia AM (2006): Cue-invariant networks for figure and background processing in human visual cortex. J Neurosci 26:11695–11708.

Babiloni F, Babiloni C, Carducci F, Romani GL, Rossini PM, Angelone LM, Cincotti F (2004): Multimodal integration of EEG an MEG data: A simulation study with variable signal-to-noise ratio and number of sensors. Hum Brain Mapp 22:52–62.

Backus BT, Fleet DJ, Parker AJ, Heeger DJ (2001): Human cortical activity correlates with stereoscopic depth perception. J Neurophysiol 86:2054–2068.

Baillet S, Mosher JC, Leahy RM (2001): Electromagnetic brain mapping. IEEE Signal Process Mag 18:14–30.

Beltrachini L, von Ellenrieder N, Muravchik CH (2011): General bounds for electrode mislocation on the EEG inverse problem. Comput Methods Programs Biomed 103:1–9.

Brewer AA, Liu J, Wade AR, Wandell BA (2005): Visual field maps and stimulus selectivity in human ventral occipital cortex. Nat Neurosci 8:1102–1109.

Bullier J (2001): Integrated model of visual processing. Brain Res Rev 36:96–107.

Busse L, Wade AR, Carendini M (2009): Representation of concurrent stimuli by population activity in visual cortex. Neuron 64:931–942.

Cohen MR, Maunsell JH (2009): Attention improves performance primarily by reducing interneuronal correlations. Nat Neurosci 12:1594–1600.

Cottereau B, Jerbi K, Baillet S (2007): Multiresolution imaging of MEG cortical sources using an explicit piecewise model. Neuroimage 38:439–451.

Cottereau B, Lorenceau J, Gramfort A, Clerc M, Thirion B, Baillet S (2011a): Phase delays within visual cortex shape the response to steady-state visual stimulation. Neuroimage 54:1919–1929.

Cottereau BR, McKee SP, Ales JM, Norcia AM (2011b): Disparity tuning of the population responses in the human visual cortex: an EEG source imaging study. J Neurosci 31:954–965.

Dale AM, Sereno MI (1993): Improved localization of cortical activity by combining EEG and MEG with MRI cortical surface reconstruction: A linear approach. J Cogn Neurosci 5:162–176.

Dale AM, Liu AK, Fischl B, Buckner RL, Belliveau JW, Lewine JD, Halgren E (2000): Dynamic statistical parametric mapping: Combining fMRI and MEG to produce high-resolution spatio-temporal maps of cortical activity. Neuron 26:55–67.

DeAngelis GC, Uka T (2003): Coding of horizontal disparity and velocity by MT neurons in the alert macaque. J Neurophysiol 89:1094–1111.
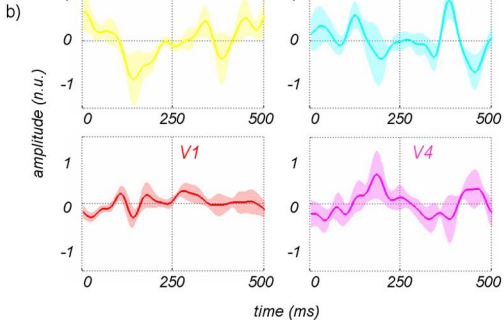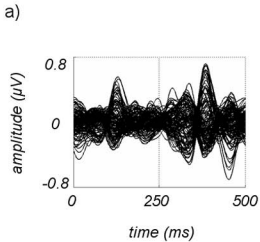
DeAngelis GC, Cumming BG, Newsome WT (1998): Cortical area MT and the perception of stereoscopic depth. Nature 394:677–680.

Di Salle F, Formisano E, Seifritz E, Linden DE, Scheffler K, Saulino C, Tedeschi G, Zanella FE, Pepino A, Goebel R, Marciano E (2001): Functional fields in human auditory cortex revealed by time-resolved fMRI without interference of EPI noise. Neuroimage 13:328–338.

Friston K, Harrison L, Daunizeau J, Kiebel S, Phillips C, Trujillo-Barreto N, Henson R, Flandin G, Mattout J (2008): Multiple sparse priors for the M/EEG inverse problem. Neuroimage 39:1104–1120.

George J, Mosher J, Schmidt D, Aine C, Wood C, Lewine J, Sanders J, Belliveau J (1995): Functional Neuroimaging by Combined MRI, MEG and fMRI. Hum Brain Mapp S1:89.

Gorodnitsky IF, George JS, Rao BD (1995): Neuromagnetic source imaging with FOCUSS: A recursive weighted minimum norm algorithm. Electroencephalogr Clin Neurophysiol 95:231–251.

Grave de Peralta R, Murray MM, Michel CM, Martuzzi R, Gonzalez Andino S (2004): Electrical neuroimaging based on biophysical constraints. Neuroimage 21:527–539.

Grova C, Daunizeau J, Lina J-M, Bénar CG, Benali H, Gotman J (2006): Evaluation of EEG localization methods using realistic simulations of interictal spikes. Neuroimage 29:734–753.

Hagler DJ, Halgren E, Martínez A, Huang M, Hillyard SA, Dale AM (2009): Source estimates for MEG/EEG visual evoked responses constrained by multiple, retinotopically mapped stimulus locations. Hum Brain Mapp 30:1290–1309.

Hallez H, Vanrumste B, Grech R, Muscat J, De Clercq W, Vergult A, D'Asseler Y, Camilleri KP, Fabri SG, Van Huffel S, Lemahieu I (2007): Review on solving the forward problem in EEG source analysis. Journal of NeuroEngineering and Rehabilitation 4(46).

Hämäläinen MS, Sarvas J (1989): Realistic conductivity geometry model of the human head for interpretation of neuromagnetic data. IEEE Trans Biomed Eng 36:165–171.

Hämäläinen M, Hari R, Ilmoniemi R, Knuutila J, Lounasmaa O (1993): Magnetoencephalography: Theory, instrumentation and applications to the non-invasive study of human brain function. Rev Mod Phys 65:413–497.

Hauk O (2004): Keep it simple: a case for using classical minimum norm estimation in the analysis of EEG and MEG data. Neuroimage 21:1612–1621.

Hinds O, Polimeni JR, Rajendran N, Balasubramanian M, Amunts K, Zilles K, Schwartz EL, Fischl B, Triantafyllou C (2009): Locating the functional and anatomical boundaries of human primary visual cortex. Neuroimage 46:915–922.

Huk AC, Dougherty RF, Heeger DJ (2002): Retinotopy and functional subdivision of human areas MT and MST. J Neurosci 22:7195–7205.

Im C, An K, Jung H, Kwon H, Lee Y (2003): Assessment criteria for MEG/EEG cortical patch tests. Phys Med Biol 48:2561–2573.

Jeffs B, Leahy R, Singh M (1987): An evaluation of methods for neuromagnetic image reconstruction. IEEE Trans Biomed Eng 34:713–723.

Jerbi K, Lachaux J, NDiaye K, Pantazis D, Leahy R, Garnero L, Baillet S (2007): Coherent neural representation of hand speed in humans revealed by meg imaging. Proc Natl Acad Sci USA 104:7676–7681.

Kenet T, Bibitchkov D, Tsodyks M, Grinvald A, Arieli A (2003): Spontaneously emerging cortical representations of visual attributes. Nature 425:954–956.

Kourtzi Z, Kanwisher N (2000): Cortical regions involved in perceiving object shape. J Neurosci 20:3310–3318.

Lampl I, Reichova I, Ferster D (1999): Synchronous membrane potential fluctuations in neurons of the cat visual cortex. Neuron 22:361–374.

Lefevre J, Baillet S (2009): Optical flow approaches to the identification of brain dynamics. Hum Brain Mapp 30:1887–1897.

Lin FH, Witzel T, Ahlfors SP, Stufflebeam SM, Belliveau JW, Hamalainen MS (2006): Assessing and improving the spatial accuracy in MEG source localization by depth-weighted minimum-norm estimates. Neuroimage 31:160–171.

Liu AK, Belliveau JW, Dale AM (1998): Spatiotemporal imaging of human brain activity using fMRI constrained MEG data: Monte Carlo simulations. Proc Nat Acad Sci U S A 95:8945–8950.

Liu AK, Belliveau JW, Dale AM (2002): Monte Carlo simulation studies of EEG and MEG localization accuracy. Hum Brain Mapp 16:47–62.

Liu Z, He B (2008): FMRI–EEG integrated cortical source imaging by use of time-variant spatial constraints. Neuroimage 39:1198–1214.

Liu Z, Zhang N, Chen W, He B (2009): Mapping the bilateral visual integration by EEG and fMRI. Neuroimage 46:989–997.

Logothetis NK (2008): What we can do and what we cannot do with fMRI. Nature 12:869–878.

Mattout J, Phillips C, Penny WD, Rugg MD, Friston KJ (2006): MEG source localization under multiple constraints: An extended Bayesian framework. Neuroimage 30:753–767.

Metz C (1986): ROC methodology in radiologic imaging. Invest Radiol 21:720–732.

Moran JE, Bowyer SM, Tepley N (2005): Multi-resolution FOCUSS: A source imaging technique applied to MEG data. Brain Topogr 18:1–17.

Mosher JC, Leahy RM, Lewis PS (1999): EEG and MEG: Forward solutions for inverse methods. IEEE Trans Biomed Eng 46:245–259.

Nunez PL, Silberstein RB (2000): On the relationship of synaptic activity to macroscopic measurements: Does co-registration of EEG with fMRI make sense? Brain Topogr 13:79–96.

Ou W, Nummenmaa A, Ahveninen J, Belliveau JW, Hämäläinen MS, Golland P (2010): Multimodal functional imaging using fMRI-informed regional EEG/MEG. Neuroimage 52:97–108.

Parker AJ (2007): Binocular depth perception and the cerebral cortex. Nat Rev Neurosci 8:379–392.

Pascual-Marqui R, Michel C, Lehman, D (1994): Low resolution electromagnetic tomography: A new method for localizing electrical activity in the brain. Int J Psychophysiol 18:49–65.

Penfield WG, Boldrey E (1937): Somatic motor and sensory representation in the cerebral cortex of man as studied by electrical stimulation. Brain 60:389–443.

Regan D. 1989: Human Brain Electrophysiology. New York: Elsevier.

Sato M, Yoshioka T, Kajihara S, Toyama K, Goda N, Doya K, Kawato M (2004): Hierarchical Bayesian estimation for MEG inverse problem. Neuroimage 23:806–826.

Schmidt DM, George JS, Wood CC (1999): Bayesian inference applied to the electromagnetic inverse problem. Hum Brain Mapp 7:195–212.

Schupp HT, Stockburger J, Codispoti M, Junghöfer M, Weike AI, Hamm AO (2007): Selective visual attention to emotion. J Neurosci 27:1082–1089.
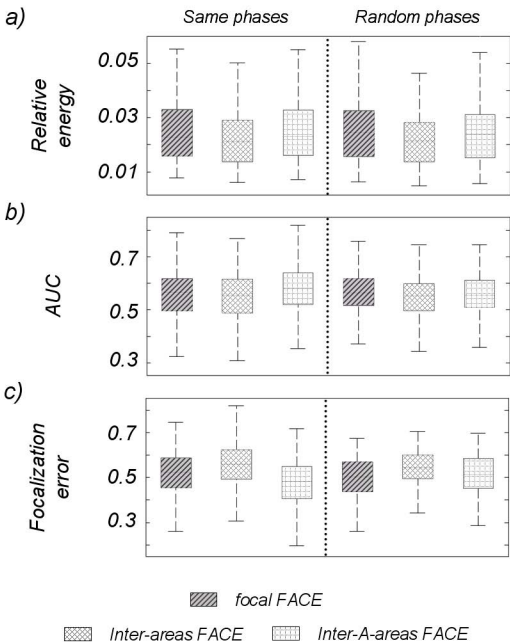
Schwartz D, Poiseau E, Lemoine D, Barillot C (1996): Registration of MEG/EEG data with MRI: Methodology and precision issues. Brain Topogr 9:101–116.

Sereno MI, Dale AM, Reppas JB, Kwong KK, Belliveau JW, Brady TJ, Rosen BR, Tootell RBH (1995): Borders of multiple visual areas in humans revealed by functional resonance magnetic imaging. Science 268:889–893.

Sergent C, Baillet S, Dehaene S (2005): Timing of the brain events underlying access to consciousness during the attentional blink. Nat Neurosci 8:1391–1400.

Smith SM (2002): Fast robust automated brain extraction. Hum Brain Mapp 17:143–155.

Tootell RB, Hadjikhani N (2001): Where is 'dorsal V4' in human visual cortex? Retinotopic, topographic and functional evidence. Cereb Cortex 11:298–311.

Trujillo-Barreto N, Aubert-Vazquez E, Valdes-Sosa P (2004): Bayesian model averaging. Neuroimage 21:1300–1319.

Tsao DY, Vanduffel W, Sasaki Y, Fize D, Knutsen TA, Mandeville JB, Wald LL, Dale AM, Rosen BR, Van Essen DC, Livingstone MS, Orban GA, Tootell RBH (2003): Stereopsis activates V3A and caudal intraparietal areas in macaques and humans. Neuron 39:555–568.

Umeda K, Tanabe S, Fujita I (2007): Representation of stereoscopic depth based on relative disparity in macaque area V4. J Neurophysiol 98:241–252.

Vanni S, Warnking J, Dojat M, Delon-Martin C, Bullier J, Segebarth C (2004): Sequence of pattern onset responses in the human visual areas: An fMRI constrained VEP source analysis. Neuroimage 21:801–817.

Vialatte FB, Maurice M, Dauwels J, Cichocki A (2010): Steady-state visually evoked potentials: Focus on essential paradigms and future perspectives. Prog Neurobiol 90:418–438.

Wade AR, Brewer AA, Rieger JW, Wandell BA (2002): Functional measurements of human ventral occipital cortex: Retinotopy and colour. Philos Trans R Soc Lond B Biol Sci 357:963–973.

Wandell BA, Dumoulin SO, Brewer AA (2007): Visual field maps in human cortex. Neuron 56:366–383.

Wang M, Gotman J (2001): The influence of electrode location errors on EEG dipole source localization with a realistic head model. Clin Neurophysiol 112:1777–1780.

Wang JZ, Williamson SJ, Kaufman L (1992): Magnetic source images determined by a lead-field analysis: The unique minimum-norm least-squares estimation. IEEE Trans Biomed Eng 39:665–675.

Wheatstone C (1838): Contributions to the physiology of vision–part the first. On some remarkable and hitherto unobserved, phenomena of binocular vision. Philos Trans R Soc Lond 128:371–391.

Wipf DP, Nagarajan S (2009): A Unified Bayesian Framework for MEG/EEG Source Imaging. Neuroimage 44:947–966.

Yoshioka T, Toyama K, Kawato M, Yamashita O, Nishina S, Yamagishi N, Sato M (2008): Evaluation of hierarchical Bayesian method through retinotopic brain activities from fMRI and MEG signals. Neuroimage 42:1397–1413.

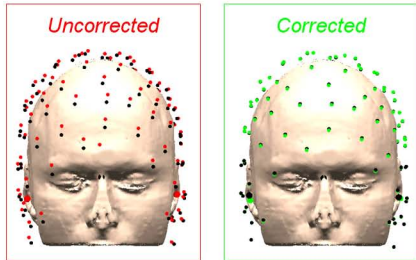a) *Relative energy*

b) *AUC*

c) *Focalization error*

Legend: □ *Minimum-norm* ▨ *auto-correlated FACE* ▨ *medium FACE* ▨ *combined FACE*

a)

Subject 4   Subject 5   Subject 6

ROIs
V1
V2
V3
V4
V3A
LOC
MT

b)

a)

b)

MT   V3A   V1   V4

a) *Relative energy*

b) *AUC*

c) *Focalization error*

Same phases | *Random phases*

focal FACE

Inter-areas FACE   Inter-A-areas FACE

a) Uncorrected   Corrected

b)

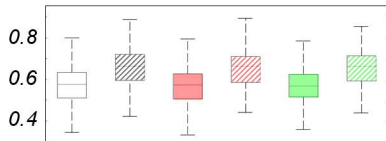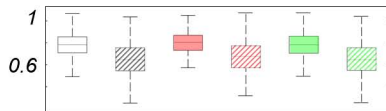*Number of electrodes*
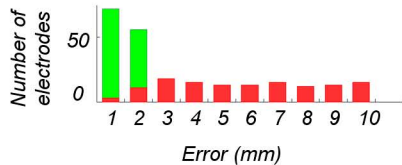
Error (mm)

c) *relative energy*
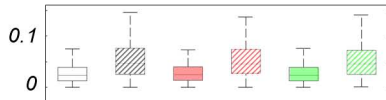
d) *AUC*

e) *focalization error*

Minimum -norm

combined FACE